A Model of Baroclinic Instability and Waves between the Ventilated Gyre and the Shadow Zone of the North Atlantic Ocean

REINER ONKEN AND BIRGIT KLEIN

Institut für Meereskunde, Kiel, Federal Republic of Germany

(Manuscript received 21 November 1989, in final form 25 June 1990)

ABSTRACT

Distributions of eddy kinetic energy in the North Atlantic Ocean show that enhanced mesoscale activity exists in the Cape Verde Frontal Zone (the eastern part of the Central Water Boundary). This variability and its associated length and time scales are investigated with a three-dimensional numerical model that uses primitive equations in a hybrid (quasi-isopycnic) coordinate system in which the Coriolis parameter varies linearly. The model has a horizontal resolution of 15.625 km in 11 isopycnic layers. The domain comprises a 1000-km square centered at 20°N having idealized bottom topography and zonally periodic boundary conditions. A zonal, geostrophically balanced jet representing an undisturbed Canary Current is used for the initial conditions. Potential vorticity is used to distinguish between water masses that are reconstructed from a hydrographic section. The growth of meanders is stimulated by an ageostrophic perturbation field consisting of white noise. Integration is carried out for 200 model days.

Baroclinic instability leads to a growth of meanders and the subsequent shedding of eddies. The most unstable wave has a length of 200 km, attains an amplitude of about 100 km after 80 model days, and sheds its first eddy around model day 140. Eddies have typical horizontal length scales of 100 km. Instabilities associated with the westward jet are confined to a zonal strip about 300 km wide and occur over time scales of 100–300 days in the uppermost layers, 100–125 days in the intermediate layers, and between 50 days and infinity in the layers close to the bottom. Baroclinically unstable waves, Rossby waves, and topographic Rossby waves contribute to the variability, but the latter two can be observed only in the layers near the bottom owing to their small amplitude relative to the growing unstable waves elsewhere.

There is good agreement between model predictions and observations with respect to the spatial scales of variability. In comparing the temporal scales predicted by the model with spectra from mooring velocity records, we find consistency within the limits imposed by statistical constraints. Phase spectra from these records indicate that the observed eddy activity in the CVFZ is due to baroclinic instability.

1. Introduction

The Cape Verde Frontal Zone (CVFZ) is the eastern part of the Central Water Boundary (CWB), which is the transition zone between North Atlantic Central Water (NACW) and South Atlantic Central Water (SACW). It extends zonally across the entire North Atlantic Ocean from the Caribbean Sea to the African coast at about 10°N, but it takes on a more southwest–northeast direction east of 30°W when approaching the African shelf (Sverdrup et al. 1942; Emery and Meincke 1986). Using the terminology of Luyten et al. (1983), the CVFZ is the boundary between the ventilated waters of the North Atlantic subtropical gyre and the "shadow zone" in the southeast, which is not ventilated by the North Atlantic.

Maps of eddy potential and kinetic energies (Dantzler 1977; Richardson 1983) in the North Atlantic reveal a zonal band of enhanced eddy activity in the region of the CWB. This relatively large variability has also been identified in the eddy-resolving circulation model of Cox (1985). Values of eddy kinetic energy in this westward flow regime of the subtropical recirculation are several times larger than in the gyre interior or in the regime of southward flow near the eastern boundary. Very strong eddy activity can be found in the CVFZ area, where the southward flow (i.e., the Canary Current) turns into the westward directed North Equatorial Current. To explain the high levels of eddy energy in this region, Cox (1985) analyzed the structure of the potential vorticity field and found the necessary conditions for baroclinic instability to be satisfied. This finding is consistent with the earlier work done by McDowell et al. (1982) and Keffer (1985), who calculated the North Atlantic potential vorticity structure based on large observational datasets. They showed that the entire westward flow regime of the subtropical gyre exhibits potential vorticity structures, which make baroclinic instability likely to occur.

Investigators from the Institut für Meereskunde in Kiel have conducted several hydrographic surveys in the CVFZ during recent years, from which first results

Corresponding author address: Dr. Reiner Onken, Institut fur Meereskunde, Düsternbrooker Weg 20, 2300 Kiel 1, Federal Republic of Germany.

have been published by Zenk et al. (1990, referred to as ZKS). These observations also show high levels of variability in the area adjacent to the eastern boundary as previously found by Manríquez and Fraga (1982), Barton (1987) and Hagen and Schemainda (1986). We conject that the observed eddy variability in the region is caused by baroclinic instability of the Canary Current. In this paper we present a numerical model whose results confirm that baroclinic instability is likely to occur in the CVFZ region, resulting in the generation and growth of meanders followed by eddy formation. Interpretations of our model results are done primarily with respect to the space and time scales of variability and are compared with recent observations.

2. The model

In our model we use a set of primitive equations in generalized vertical coordinates. These equations have been derived by Bleck (1978) and applied by Bleck and Boudra (1981, referred to as BB) in their ocean circulation model. Our model code and the nomenclature are identical to BB, hence only deviations from that model will be described in this section.

a. Boundary conditions, technical details and parameters

Our model domain is a 1000 km × 1000 km square bounded in north ($x = 0$) and south ($x = L$) by solid walls. In the y-direction (west–east, y positive to the east) the box is limited at $y = 0$ and $y = B$; L will be referred to as "cross-front scale" and B as "along-front scale." Bottom topography is variable, but only in the x-direction, representing the rise of the Cape Verde Plateau. The boundary conditions at $x = 0$ and $x = L$ are $u = 0$ and $\partial v/\partial x = 0$ (free slip, u and v are the components of the horizontal velocity vector in x- and y-direction, respectively), in y-direction periodic boundary conditions are applied. The boundary conditions for the sea surface and the bottom are those for material surfaces, i.e., $\dot{s}\partial p/\partial s = 0$. Here, p is the pressure and s represents the generalized vertical coordinate. The model domain is partitioned into 64 equally spaced grid intervals $\Delta x = \Delta y = 15.625$ km on 11 layers of constant potential density. The minimum layer thickness allowed to be attained during the model integration has been set to $\Delta p_0 = 2$ db. A horizontal eddy viscosity coefficient $\nu = 600\ \mathrm{m^2\ s^{-1}}$ has been chosen to reduce small "numerical" waves. High frequency fluctuations in the velocity field are damped by a three-point (0.25-0.5-0.25) time smoother. The Coriolis parameter f varies linearly in north–south direction as $f = f_0 + \beta(x - L/2)\cos(45°)$, where f_0 is the Coriolis frequency at 20°N latitude and $\beta = \partial f/\partial x$. Explanation of the cos(45°)-term is given in section 2b. The time step is 26 minutes.

b. Initial conditions

As initial conditions we define a zonally independent mass field having a westward geostrophic jet representing the unperturbed Canary Current. In order to stimulate the growth of meanders, a small amplitude ageostrophic perturbation velocity field is superimposed on that basic state.

Our initial mass field is specified on the basis of one of the CTD sections presented in ZKS. We have elected to use section B (ZKS, Fig. 6) because a water mass analysis (ZKS, Figs. 10, 11) reveals that in the northern part there is about 90% NACW, whereas in the southern part there is 90% SACW. This is not the case in section A, which is dominated by NACW excepting for a narrow band of SACW. Thus, section B may best represent the transition between SACW and NACW, i.e., the two-water-mass front in the classical sense.

The crucial parameter controlling the dynamical behavior of a stratified fluid on a rotating sphere is the isopycnic potential vorticity gradient IPVG (Hoskins et al. 1985). So, when adjusting the initial mass field of the model to the section B mass field, it is of first order importance to conserve the IPVG structure. The easiest way to do that is to copy the observed mass field exactly into the model, but this would give rise to interaction of the artificial channel walls with the fluid in the interior because of non-zero geostrophic velocities at $x = 0$ and $x = L$. On the other hand, section B cannot represent the ideal basic state of the water mass boundary. The water mass analysis in ZKS revealed a high degree of large-scale mixing between SACW and NACW, which we suppose to be the consequence of a turbulent eddy field driven by baroclinic instability. In order to overcome both problems, we analyzed the isopycnic potential vorticity (IPV) of section B and estimated the IPV contrast between NACW and SACW before the front would become unstable. We then constructed a smooth transition between SACW and NACW by using a hyperbolic tangent function.

Results of this procedure are displayed in Figs. 1 and 2. Figure 1a shows the density field along section B; Fig. 1b, the model density field and associated geostrophic velocities. We have plotted only those isopycnals which coincide with s surfaces in the model, i.e., the vertical resolution of the model is 0.3 σ_θ-units. As a consequence of the hyperbolic tangent fit several details of the observational data have been lost, for example the doming of the isopycnals at station 315 and the outcropping of the $\sigma_\theta = 25.1$ isopycnal at station 317. The frontal jet is now confined to the center of the model domain; peak velocities are $-9.8\ \mathrm{cm\ s^{-1}}$. Below about 400 m depth a weak return flow of roughly $1\ \mathrm{cm\ s^{-1}}$ can be found. Figure 2 shows the IPV distribution on the 11 potential density surfaces in section B and in the model, both in the physical units used in the model. In s coordinates IPV is defined as

$$\text{IPV} = \frac{\zeta + f}{\partial p / \partial s} \qquad (1)$$

Here, $\zeta = (\partial v/\partial x)_s - (\partial u/\partial y)_s$ is relative vorticity and $\partial p/\partial s$ the pressure gradient between the s surfaces on top and at the bottom of each s layer. We have neglected the relative vorticity contribution in computing IPV values from the observational data. But from ZKS (Fig. 14), we have estimated the ζ/f contribution to be only on the order of 1%. In order to adjust the model as close as possible to the observed field, it would have been appropriate to rotate the model domain by an angle of about 45° counterclockwise. This would have aligned section B perpendicular to the solid model boundaries at $x = 0$ and $x = L$. But that means the Coriolis parameter would have to depend on both x and y. This is impossible because of the cyclic model boundary conditions in the y-direction. To overcome this problem we have reduced the β-term by a factor of cos(45°). The result is that f changes by the same amount across the front in both the model and in the observational data. This allows us to compare the IPV structures in the observed and modeled sections in Fig. 2. The observational data exhibit three different IPV regimes: In layers 1 to 6 there is low IPV in the north and higher IPV in the south. This is consistent with potential vorticity structures in this area mapped by McDowell et al. (1982) and Keffer (1985), and with Cox's (1985) potential vorticity analysis. The opposite is found in the four layers below where the IPV decreases from higher to lower latitudes. Finally, in the bottom layer, the meridional gradient of IPV once again changes sign. A comparison of the IPV structure in the upper layers with ZKS's Fig. 11 reveals that high values of IPV seem to be correlated with SACW, and low values with NACW. Qualitatively the same structures are found in the model IPV field, but here we have specified a water mass configuration that might have existed prior to any adjustments to instabilities, i.e., low IPV in the north and high IPV in the south in layers 1 to 6, and the reversed trend in the layers

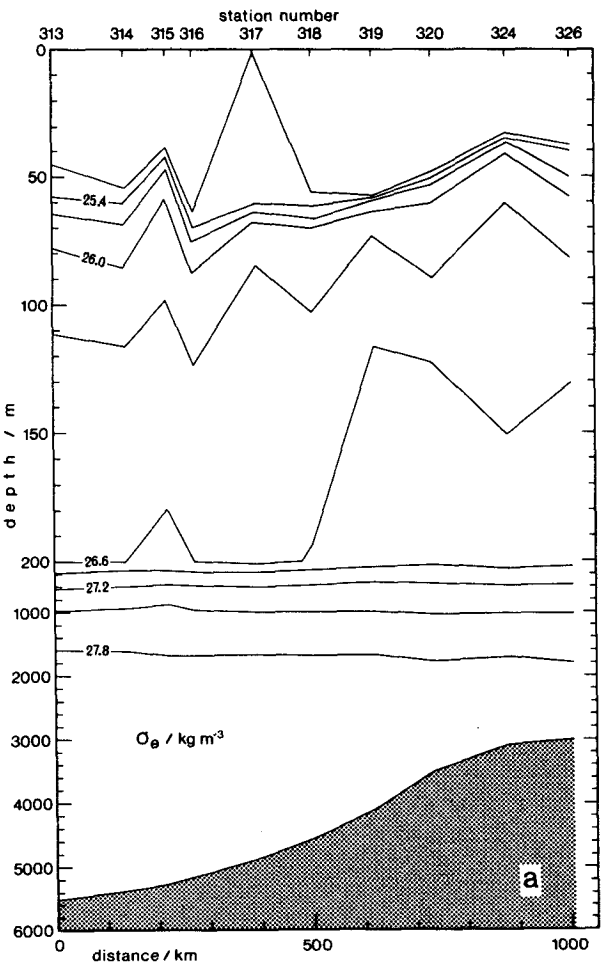

FIG. 1a. Potential density field along CTD section B from ZKS. The bottom is indicated by shading.

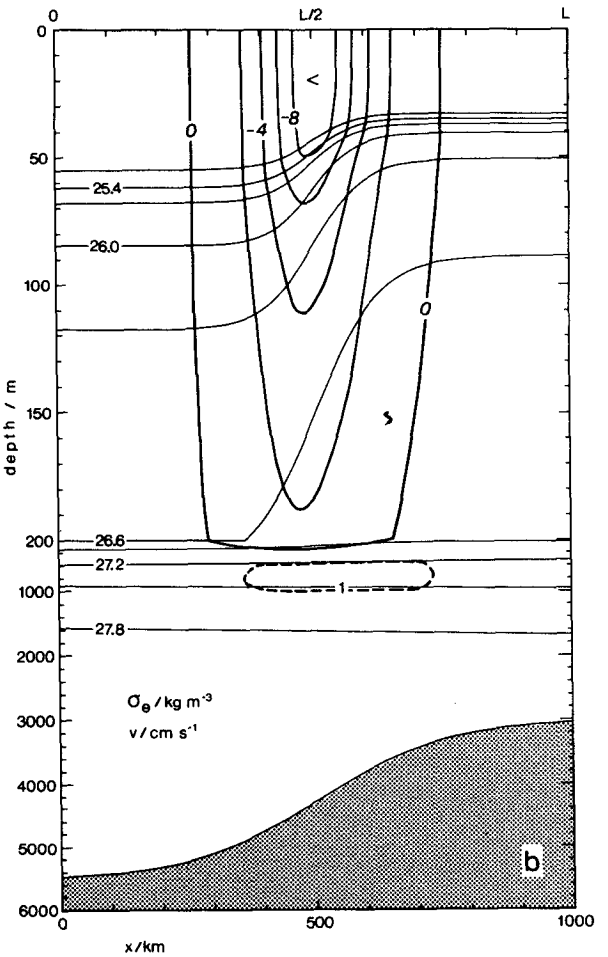

FIG. 1b. Initial model potential density field (thin lines) and isotachs of the geostrophic jet (heavy lines). Broken lines denote eastward flow.

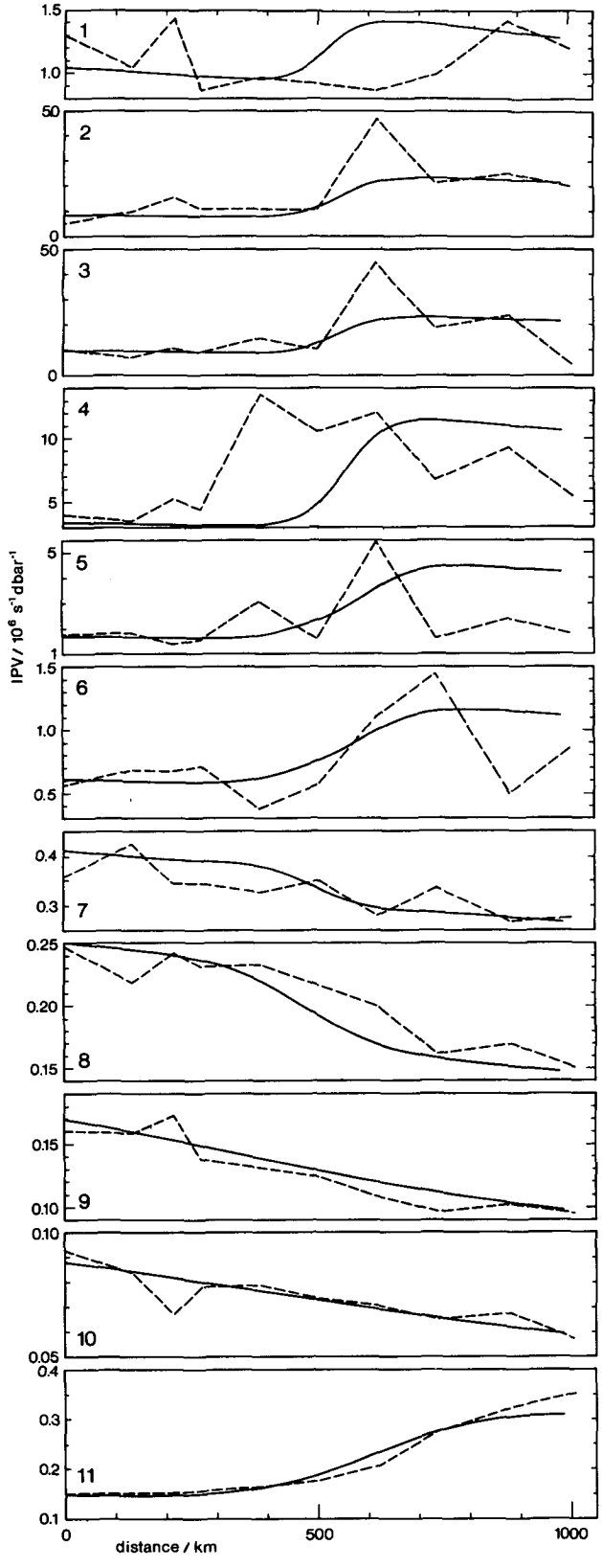

FIG. 2. Distributions of isopycnic potential vorticity on the 11 isopycnals in CTD section B from ZKS (broken lines) and in the model (solid lines). See text for explanation of the physical units.

below except the bottom layer. Summarizing, the IPV difference evaluated between $x = 0$ and $x = L$ clearly changes sign with depth, not once but twice, each in the observational dataset and in the model IPV field. The necessary condition for baroclinic instability is therefore satisfied.

c. *The perturbation field*

Because the initial mass and flow fields in the model are identical in every cross-front section, meanders on the front can form and grow only if a perturbation is superimposed. In order to enable the most unstable wave length to grow from the very outset, a white-noise random-phase perturbation field is defined in each layer in terms of an ageostrophic u-field varying sinusoidally in the y-direction:

$$u = u_0\left[a_1 \exp\left(a_2 \frac{x}{L} + a_3 \frac{x^2}{L^2}\right) - a_1\right] \times \sum_{i=1}^{32} \sin\left(2\pi k_i \frac{y}{B} + \mu_i\right) \quad (2)$$

where $u_0 = 1$ mm s^{-1} is the single Fourier component perturbation amplitude, $k_i = B/\lambda_i$ the channel wavenumber, λ_i the corresponding wave length and μ_i the random phase in the range $0 < \mu_i < 2\pi$. The function enclosed in brackets using the coefficients $a_1 = 10^{-8}$, $a_2 = 4 \ln a_1$, and $a_3 = -a_2$ is symmetric about $x = L/2$. There it has a maximum value of nearly 1 and decays monotonically towards zero approaching the channel sidewalls. Hence the perturbation is strongest, where the jet has its maximum speed and does not violate the solid wall boundary condition at $x = 0, L$.

3. Model results

We have integrated the model over 200 days. This is an appropriate time scale for looking at the evolution and shape of baroclinic disturbances because of two reasons: First, the general circulation pattern in the CVFZ exhibits a strong seasonal variability due to the intensification of the North Equatorial Counter Current in summer and fall (Richardson and Walsh 1986). This is equivalent to having boundary conditions that vary seasonally, in which case the assumption of a free jet in the absence of any external forcing may no longer hold. Second, there is an intense diabatic forcing in this area due to solar irradiance, which changes the potential vorticity field in the upper layers. IPV conservation cannot be claimed under such conditions, and even 200 days might be too long for an integration period. We only can postulate that the qualitative structure of the potential vorticity field does not change significantly within this period of time.

a. *Evolution and structures of the flow field*

Figure 3 shows a sequence of upper-layer streamfunction fields. On day 0 the streamlines are strictly

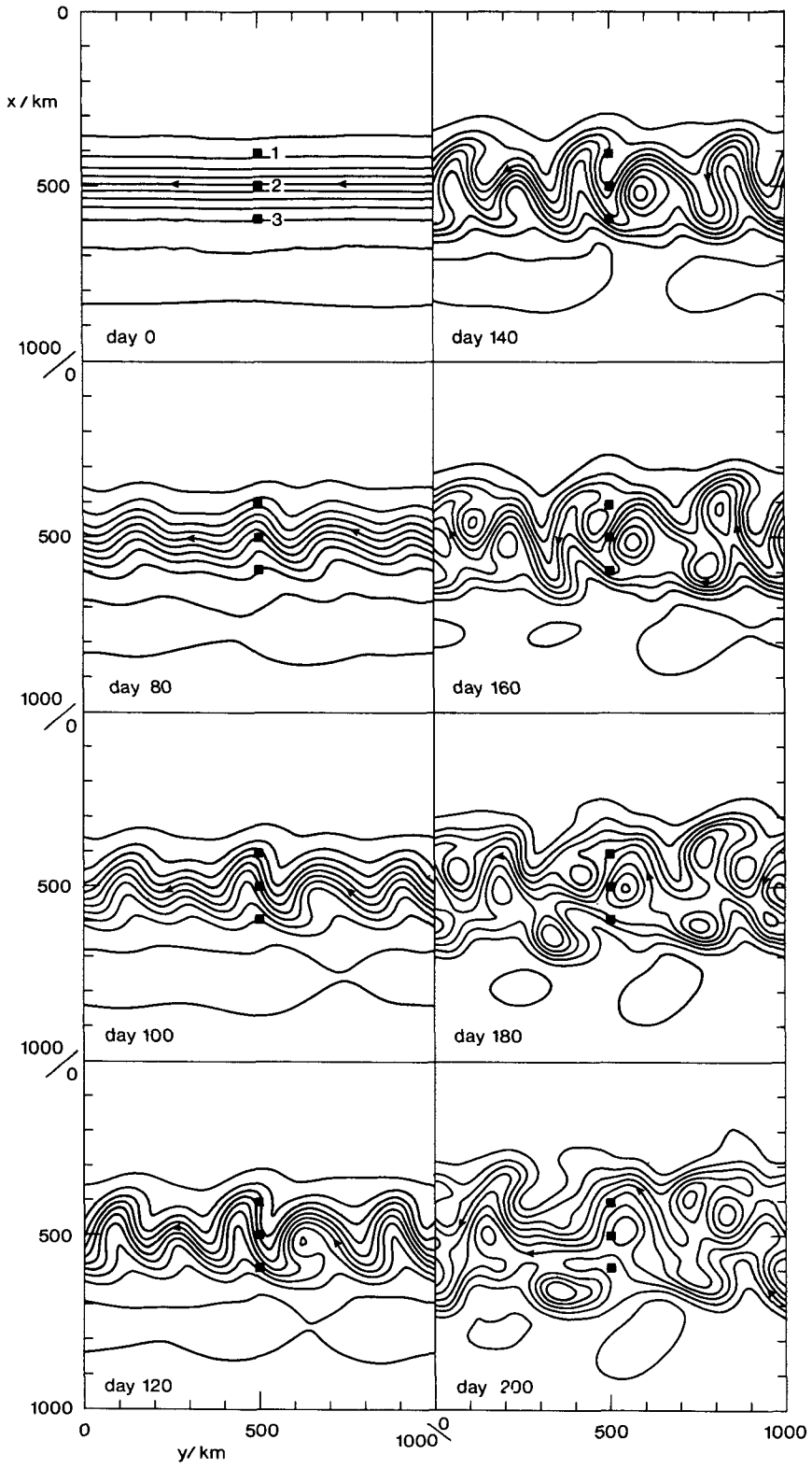

FIG. 3. Temporal evolution of the streamfunction in the uppermost layer. The contour interval is 2000 $m^2 s^{-1}$. Squares indicate positions of the model moorings.

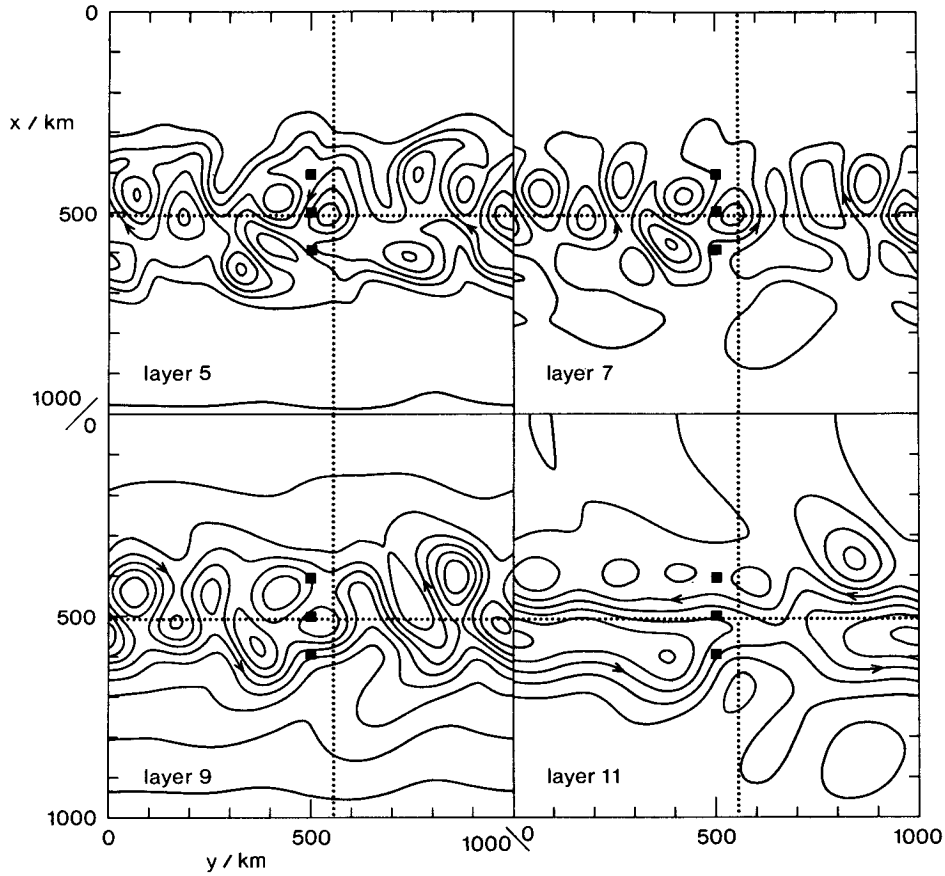

FIG. 4. Streamfunction fields in 4 different layers on day 180. Squares indicate positions of model moorings. Contour interval is 2000 $m^2 s^{-1}$ in layer 5, 1500 $m^2 s^{-1}$ in layer 7, 1000 $m^2 s^{-1}$ in layer 9, and 200 $m^2 s^{-1}$ in layer 11. Dashed lines refer to the location of the sections shown in Fig. 5.

zonal except for small deviations caused by imposing the specified perturbation on the basic state. After 80 days meanders having peak-to-trough ranges of about 100 km have developed. The dominant meander wave length is about 200 km. Meander growth continues to day 160 when for the first time eddies become detached to the north and south of the meandering jet. A characteristic feature during this growth phase is the backward breaking of the meanders, which can be seen very clearly on days 120 and 140. A comparison of subsequent positions of meander troughs and ridges during this time period gives a meander phase speed of about 2 cm s^{-1} westward.

After day 160 several eddies have become detached from the front to the north (cyclones) and to the south (anticyclones). Beginning with day 180, the initial jet has been split up into an eddy field which has a north–south extent of roughly 300 km. The eddies are typically 100 km across and behave in similar ways regardless of whether they are cyclonic or anticyclonic; once they are detached from the frontal jet, they do not propagate any farther to the north or south, but keep in touch with the unstable region or are even reentrained into the frontal zone. This confines the instabilities to a 300 km wide strip which is also the case when the model is integrated up to day 300.

Shown in Figure 4 are contemporaneous streamfunction fields in 4 different layers on day 180. Layer 5 exhibits very nearly the same flow field characteristics as layer 1 (compare with Fig. 3), with only the magnitude of the currents being weaker. Also, the flow in layers 7 and 9 show a high degree of correlation with the layers above. A completely different flow pattern can be seen in the bottom layer (layer 11): Instead of a strongly meandering jet, the flow field is dominated by two bands of zonal flow to the west near the middle latitude of the model domain and to the east in the southern half. Closed streamline contours are found only in the regions peripheral to the zonal bands. The centers of these "eddies" coincide roughly with the corresponding eddy centers above but the strength of the eddy flow with respect to the mean flow is very much weaker in this layer. In addition, there are more anticyclonic eddies than cyclonic. Another fundamental difference is that the meridional extent of the eddy field is not limited to the 300-km zonal strip as in the layers above, but touches the northern and southern walls of the model domain. The eddy axes are orien-

tated in a northwest–southeast direction in the northern half of the model domain and in a southwest–northeast direction in the southern half.

Additional information concerning the structure of the flow field can be obtained from vertical sections of velocity. Figure 5 shows sections of the zonal and meridional components of flow on day 180 using potential density as vertical coordinate. In comparison with the initial structure (Fig. 1b) there is an overall increase in magnitude of the flow in all layers. Maximum speeds of more than 10 cm s^{-1} can be found in the layers close to the surface. In the layers below 400-m depth ($\sigma_\theta > 26.9$ kg m^{-3}) typical velocities now are greater than 5 cm s^{-1} instead of nearly no motion at the beginning of the integration. Both velocity components change sign across the sections on scales of about 100 km. Also, the velocity components are not completely coherent in the vertical. There are sign changes in direction that occur primarily in the density range $26.9 < \sigma_\theta < 27.4$, which is equivalent to a depth range between about 400 and 800 m (compare with Fig. 1b).

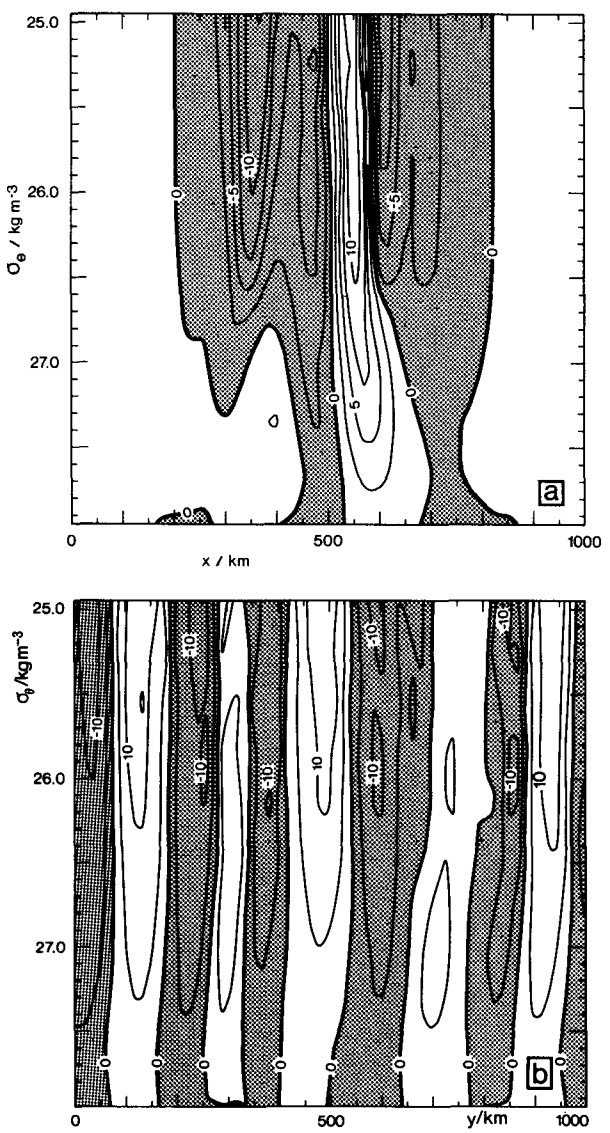

FIG. 5. Vertical sections of velocity on day 180 in isopycnic coordinates. Positions of the sections are shown in Fig. 4. (a) Zonal velocity at $y = 555$ km. Shading indicates westward flow. Contour interval is 2.5 cm s^{-1}. (b) Meridional velocity at $x = 508$ km. Shading indicates northward flow. Contour interval is 5 cm s^{-1}.

b. Variability of the flow field at selected locations

To obtain information about the temporal variability of the flow field, we have positioned an array of three "moorings" across the frontal zone, each having a "current meter" in the centers of layers 1, 5, 7, 9, and 11. The positions of the model moorings are denoted by squares in Figs. 3 and 4 and labeled by numbers in Fig. 3 on day 0. Time series of the horizontal velocity vectors recorded by those current meters are displayed in Fig. 6.

Referring first to the time series from mooring no. 2 in the center of the jet (Fig. 6b), the currents in layers 1 and 5 exhibit nearly the same characteristics. During the initial 10 days of integration the velocity vectors points to the west. Afterwards they rotate counterclockwise up to about day 60, where we find a maximum southwesterly flow of about 10 cm s^{-1}. Between days 60 and 115 the vectors rotate clockwise; a maximum flow of nearly 20 cm s^{-1} directed to the north-northwest occurs around day 110. This is twice the initial maximum velocity (compared with Fig. 1b). Starting at about day 115 the velocity vectors again rotate counterclockwise up to the end of the integration at day 200. The period between days 140 and 200 is dominated by flow to the south-southwest. Qualitatively, the same behavior can be found in layer 7, but here the flow is only half as strong as in layers 1 and 5 with the rotation of the velocity vector being shifted in phase. This phase shift varies between 10 and 25 days. At first glance the same appears to happen in layer 9, but now the vectors point to the southeast during the first 50 days and the first sign change of the meridional component occurs at about day 50 accompanied by counterclockwise rotation. The second sign change at about day 110 occurs again by counterclockwise rotation as in the layers above. As before, the rotation is phase shifted by another 10 to 20 days as compared with layer 7. Except for the differences mentioned so far, the flow in layers 1, 5, 7, and 9 have one common feature—a well defined oscillation period of about 150 days. This period can also be found in the bottom layer, but a second and shorter one of about 50 days is also evident.

Both of these periods, 150 and 50 days, can also be identified in the bottom layer current meter records from moorings 1 and 3. The vertical coherencies among the other layers of those moorings are qualitatively similar as at mooring site 2: There is a rather strong coherence between the current signals in layers 1, 5, and 7 during the first 150 days of the integration, but

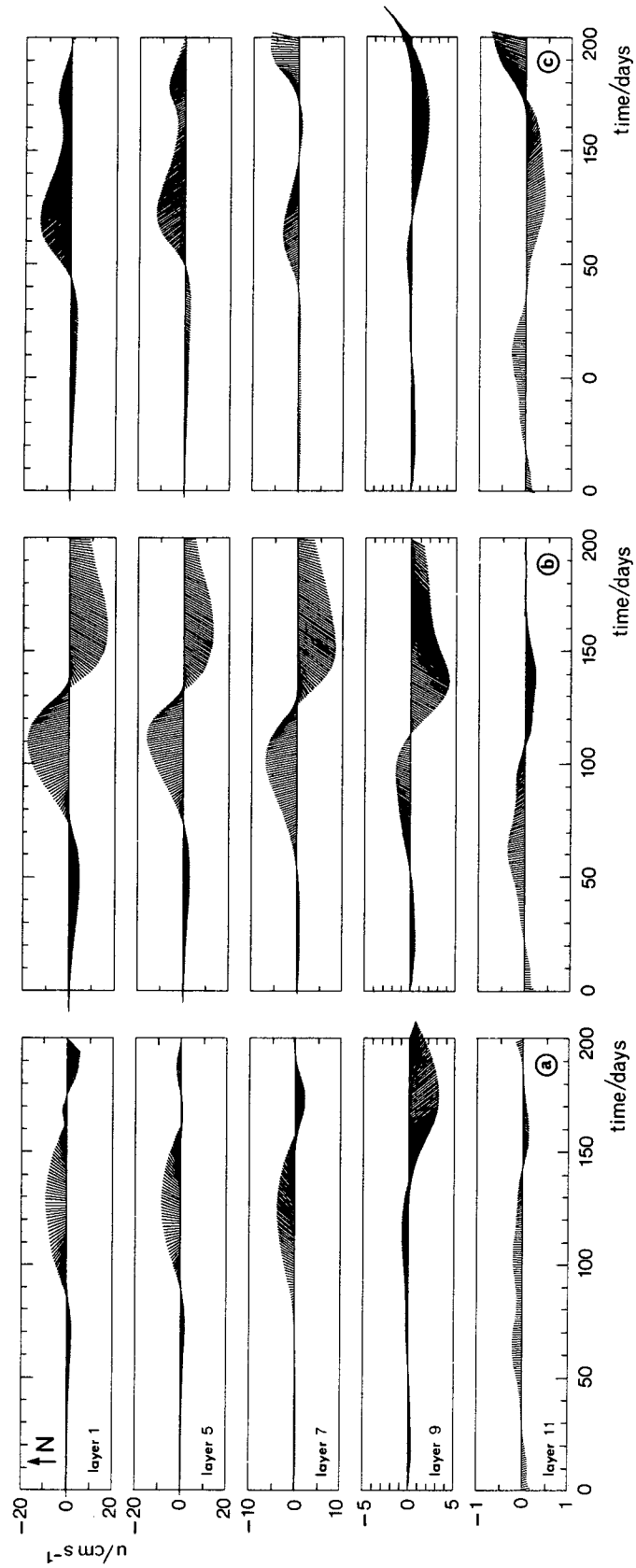

FIG. 6. Time series of the horizontal velocity vector in different layers in the model at three mooring locations. The locations of the model moorings are denoted by squares in Figs. 3 and 4. (a) Mooring 1: $x = 398$ km, $y = 492$ km; (b) Mooring 2: $x = 492$ km, $y = 492$ km; (c) Mooring 3: $x = 586$ km, $y = 492$ km.

afterwards these layers become more and more decoupled. As at mooring 2, the 9th layer currents at moorings 1 and 3 evolve in a different manner as those lying above. A comparison between the currents at 2 in the center of the jet and moorings 1 and 3 at the northern and southern flanks reveals that the dominant time scales of variability in the regions peripheral to the jet are different from those found in its center; at mooring 2 there are typical scales of about 150 days, whereas the variability at the other sites seems to be dominated by scales between 60 and 100 days or even shorter.

c. *Growth and propagation of waves*

In the preceding section we have estimated by eye the time scales of variability in the velocity time series as being in the range of about 50 to 150 days. In order to identify the physical processes leading to such scales we have performed a Fourier decomposition of the u-component (cross-frontal velocities) at $x = L/2$ in each layer at 24-hour intervals and have derived time series of the amplitude and phase speed of all Fourier component; this decomposition is possible only because we have used periodic boundary conditions. It is a common feature of nonlinear systems that unstable waves "vascillate," i.e., they do not grow continuously; after a certain period of growth comes a reduction in wave amplitude, which is followed by another growth cycle (Hide and Mason 1975). At the moment when the growth rate changes sign there are phase jumps, which, for a short period of time, lead to anomalous phase velocities as revealed by Fourier analysis. Because we are interested only in the gross properties of the waves, we have averaged the amplitude and phase speed of every Fourier component over the entire integration interval of 200 days. These averaged quantities are displayed in Fig. 7.

Figure 7a shows $\bar{u}$, the mean amplitude of cross-frontal current velocity for every wavenumber in each layer. For clarity we have included the corresponding zonal wave lengths on the upper horizontal axis and the layer mean depths on the right vertical axis. Because all wavenumbers initially had the same perturbation amplitude of $u_0 = 1$ mm s^{-1} (see section 2c). this contour plot provides an impression of how each Fourier component in the various layers grows; the contour values are in fact growth factors. We have terminated the spectrum at wavenumber 10, thus there is no growth for shorter waves. In layers 1 through 8 maximum growth occurs for the 200 km wave. In the deeper layers the wavelength with the maximum amplitude is 250 km. The most striking difference between the upper and the lower layers is that there is a well-defined spectral peak in the upper layers near wavenumber 5 together with strong amplitude gradients in wavenumber space, whereas in the deeper layers we find a nearly white spectrum.

Figure 7b shows the spectrum of the phase speeds $\bar{c}$. For clarity we have partitioned the spectrum into three regimes: Regime I (dark shading) has small (<1 cm s^{-1}) positive phase speeds, i.e., the waves travel to the east. These waves are generally less than 333 km long and can be found only in layers 9, 10, and 11. Regime II (light shading) is characterized by long (>333 km) waves moving very fast to the west. Their phase speeds are in the range of -5 to -30 cm s^{-1}. These waves can only be found below layer 3. The rest of the spectrum (Regime III, white), the major portion of it, has slower westward travelling waves. Their phase speeds are bounded by -5 and 0 cm s^{-1}. In layers 1, 2, and 3 these waves occupy the entire wavenumber spectrum, whereas in the layers below they have a long wave limit of around wavenumber 2 and in layers 9 and below they are also limited at the short wave end. This short wave limit is wavenumber 9 in layer 9, wavenumber 6 in layer 10 and wavenumber 3 in the bottom layer. Thus the bandwidth of Regime III decreases from 10 wavenumbers in the surface layers to only one wavenumber in the bottom layer.

In order to compare the model spectra with measurements from actual current meter moorings, we have calculated the modeled wave periods $\bar{\tau}$ from their lengths and phase speeds (Fig. 7c). In this figure we have also partitioned the spectrum into three regimes. Regime I is the low-frequency regime (dark shading) having periods greater than 300 d. These long periods can be found in layers 9, 10, and 11 for wavenumbers greater than 3 and in layers 1 to 6 at the low wavenumber end. The middle-frequency Regime II (periods between 150 and 300 d, light shading) is located between wavenumbers 1 and 5 in layers 1 to 7 and somewhere between wavenumbers 2 and 10 in layers 8 to 11, but here it is only poorly defined. The rest of the spectrum is what we call the high-frequency Regime III (white) having periods shorter than 150 d. This regime can be found in the high wavenumber range in the upper layers and at the other end of the spectrum in the lower layers. Hence the spectrum is arranged in such a way that in the upper layers (1 to 7) the long periods are associated with low wavenumbers and the short periods with higher wavenumbers. The opposite holds in the deeper layers, where low wavenumbers have short periods and high wavenumbers have longer ones.

Thus far we have not addressed questions as to which waves are important in determining the spectrum of variability. In order to do that, we have scaled in every layer the amplitude of each wavenumber (Fig. 7a) by the maximum amplitude occurring in that layer. Those amplitudes reaching at least 40% of the maximum layer amplitude are contained within the dashed lines in Fig. 7c. Now we can confirm our observations of the dominant periods in our modeled mooring records (Fig. 6): The most important periods in the upper layers are between about 100 and 300 days with a peak occurring at roughly 150 days. With increasing layer depth the

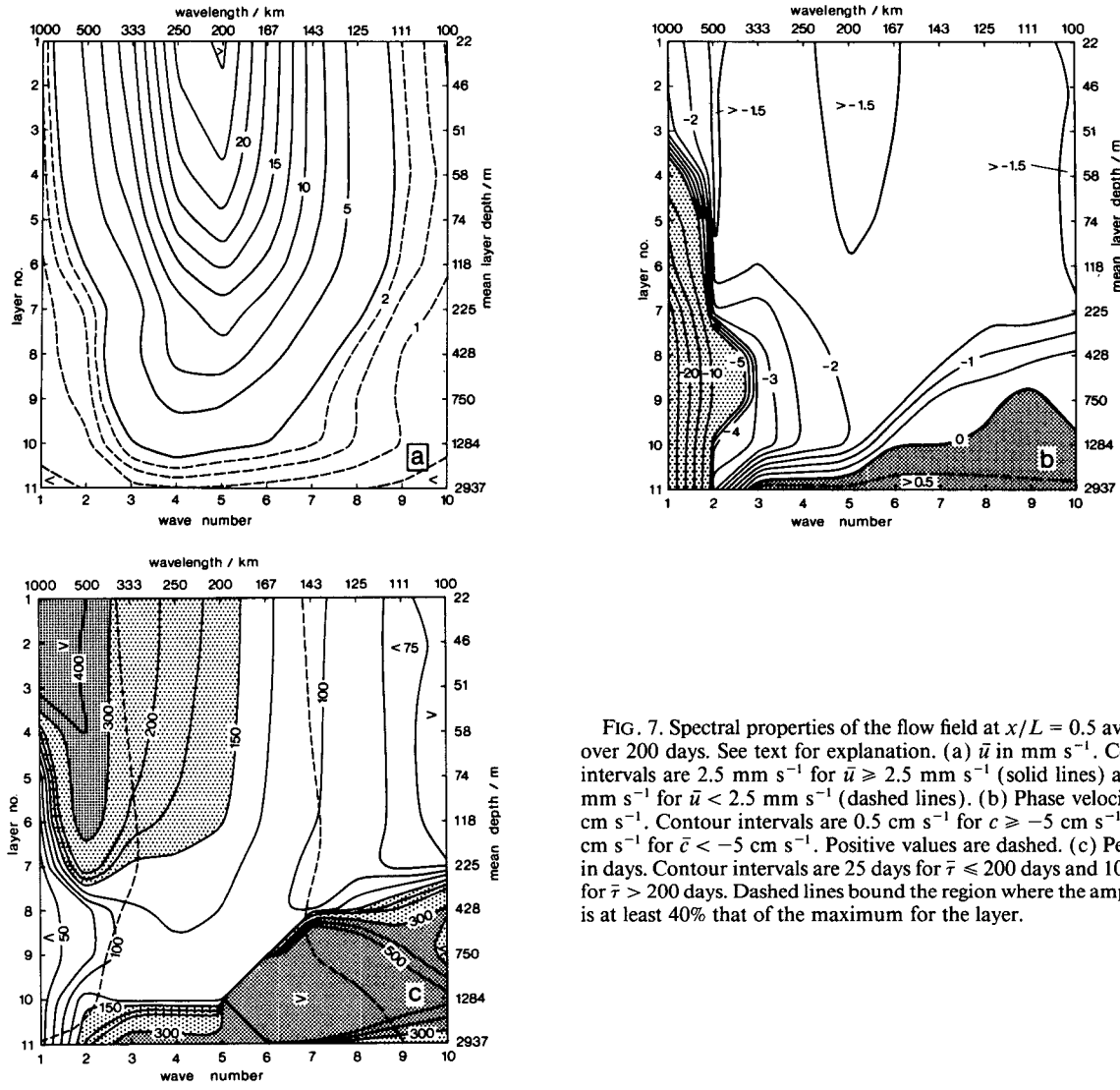

FIG. 7. Spectral properties of the flow field at $x/L = 0.5$ averaged over 200 days. See text for explanation. (a) $\bar{u}$ in mm s^{-1}. Contour intervals are 2.5 mm s^{-1} for $\bar{u} \geq 2.5$ mm s^{-1} (solid lines) and 0.5 mm s^{-1} for $\bar{u} < 2.5$ mm s^{-1} (dashed lines). (b) Phase velocity $\bar{c}$ in cm s^{-1}. Contour intervals are 0.5 cm s^{-1} for $c \geq -5$ cm s^{-1} and 5 cm s^{-1} for $\bar{c} < -5$ cm s^{-1}. Positive values are dashed. (c) Period $\bar{\tau}$ in days. Contour intervals are 25 days for $\bar{\tau} \leq 200$ days and 100 days for $\bar{\tau} > 200$ days. Dashed lines bound the region where the amplitude is at least 40% that of the maximum for the layer.

range of important periods becomes narrower; in layers 7 and 8, for example, only periods between 100 and 125 days contribute significantly to the variability. In the deeper layers the spectrum once again broadens: layers 9 and 10 are characterized on the one hand by periods between 100 and 125 days in the wavenumber range between 2 and 5, and, on the other hand, by shorter waves having periods even longer than a year. Finally, in the bottom layer we find the full range of periods contributing to the spectrum of variability: wavenumbers greater than 3 have periods longer than 300 days whereas the lower wavenumbers 1 and 2 have periods from about 200 days to less than 50 days which is the high-frequency spectral band that we previously observed in the bottom layer time series.

d. Energetics

We have not yet confirmed baroclinic instability to be the physical mechanism leading to the eddy activity at the model. This is done with Fig. 8, which shows time series of different types of energy conversions calculated according to Boudra et al. (1988) and integrated over the entire model domain. The conversion of potential to kinetic energy (PK) contains a high frequency oscillation during the first 20 days of integration that indicates the initial mass and flow fields are not well balanced which in turn is probably an effect of the ageostrophic perturbation. Later PK rises monotonically to about day 120, where it reaches a relative maximum of nearly 0.08 mW m^{-2}. For approximately the next 50 days PK decreases again and becomes even negative for about 20 days before a new growth cycle begins. An absolute maximum PK occurs on day 200 of more than 0.08 mW m^{-2}. The conversion of potential to eddy kinetic energy (PK′) is nearly in phase with PK, but is weaker. The difference PK − PK′ is balanced by P$\bar{\text{K}}$, which is the conversion of potential to mean kinetic energy. P$\bar{\text{K}}$ is always positive, indicating that the mean flow is continuously fed from

the potential energy reservoir. But this is not the only source; the mean flow is also supported by negative $\bar{K}K'$. This means that the mean flow is permanently extracting energy from the eddy kinetic energy field, or, in other words, the flow is barotropically stable. Baroclinic instability is the only source for the meander growth and eddy production.

4. Discussion

The computation of energy conversions has confirmed that in our model baroclinic instability is the main physical mechanism for meander growth and eddy generation. This could already be conjectured from the phase shift of the velocity vector with depth (Fig. 6b), which is a necessary condition for potential energy release by baroclinic instability (Pedlosky 1979). This is not surprising since the necessary conditions for baroclinic instability (cf. Gill 1982) have been satisfied twice in the model: The IPVG changes sign for the first time between layers 6 and 7, i.e., the IPV is high in the south and low in the north for σ_θ less than 26.6 kg m^{-3}. The second sign change occurs in the bottom layer due to the bottom slope of the Cape Verde Plateau. But which of those sign changes drives the instability? In order to answer this question, we repeated our model run without sloping topography but with a flat bottom at 5500-m depth. This only causes the meanders to grow more slowly, which can be seen when comparing the energy conversion rates of both runs. The graphs of the conversion rates are rather similar, but in the flat bottom case the maxima of the baroclinic conversions PK and PK′ are shifted in time by about 25 days, resulting in the maximum release of potential energy to occur around day 150 (cf. Fig. 8). Hence, we can conclude that the sloping bottom, by itself, is not the primary source for the instability, but only accelerates the growth of perturbations. This destabilizing effect of a sloping bottom is in agreement with findings by Orlanski (1969), Mechoso (1981) and Ikeda (1983), all of whom investigated this problem with two- and three-layer quasi-geostrophic models.

The most unstable wave in our standard run has a wavelength of 200 km. This is in excellent agreement with predictions by Eady's baroclinic instability model (cf. for example Le Blond and Mysak 1978, §7). If we assume a constant vertical shear and zero flow at the bottom, then the phase speed of baroclinic disturbances is given by

$$c = \frac{U_0}{2} \pm \frac{U_0}{\kappa}\left[\left(\frac{1}{2}\kappa - \tanh\frac{1}{2}\kappa\right)\left(\frac{1}{2}\kappa - \coth\frac{1}{2}\kappa\right)\right]^{1/2} \tag{3}$$

Here, U_0 is the horizontal velocity at the sea surface and

$$\kappa = r(k^{*2} + n^2\pi^2/L^2)^{1/2}, \tag{4}$$

with r being the internal Rossby radius of deformation, k^* the wavenumber, L the channel width and $n = 1, 2, 3, \cdots$. The waves are unstable whenever the radicand in (3) is negative, which is approximately the case for $\kappa < 2.4$. According to Emery et al. (1984), the internal Rossby radius in our area (20°N, 30°W) is about 50 km. Then, for the gravest mode in our model ($n = 1$ and $L = 1000$ km) the Canary Current should be unstable for wavelengths greater than about 130 km. We find in fact no growth for wavelengths shorter than 100 km (cf. Fig. 7a). The growth rate of unstable waves is given by

$$k^* c_i = \frac{U_0 k^*}{\kappa}\left[\left(\frac{1}{2}\kappa - \tanh\frac{1}{2}\kappa\right)\left(\coth\frac{1}{2}\kappa - \frac{1}{2}\kappa\right)\right]^{1/2}. \tag{5}$$

For the parameters used in our model, maximum growth can be found for wavelengths around 200 km, in excellent agreement with our model findings.

We do not expect our spatial scales of variability to be altered dramatically in a flat bottom channel, because the stratification is confined to the near surface regions and a change of bottom topography does not affect significantly the internal Rossby radius. In fact, a comparison of both runs shows that the spatial scales are identical. This is true not only for the wavelengths of the meanders, but also for the eddy scales and the meridional extent of the unstable region in all layers except the bottom layer. However, in contrast to the standard run in which there is a banded structure of the flow field, there are no bands produced in the flat bottom case. But the northwest–southeast orientation of the eddies in the northern half and the southwest–northeast orientation in the southern half of the model domain is still present. This suggests that the banded structure of the flow field in the bottom layer in the standard run is caused by topographic Rossby waves, which can exist only in the presence of a sloping bottom. We have also tested the sensitivity of our spatial scales with respect to the varying Coriolis parameter. A repetition of our model run with a constant Coriolis frequency of 4.97×10^{-5} s^{-1} instead of the linearly varying one, reveals that in the upper layers the spatial scales of the eddies do not change. However, the instabilities are no longer limited to a zonal band; after 200 days of integration the meanders have nearly reached the north and south model walls. According to Haidvogel (1983), the meridional scale of the turbulent flow (i.e., the width of the eddy field) should be of order $(2U/\beta')^{1/2}$, where U is the rms horizontal velocity and $\beta' = \beta\cos(45°)$. In our model U is of order 0.1 m s^{-1}, thus the width of the eddy field should be of order 100 km, which agrees rather well with our model results. In the same run, the northwest–southeast and southwest–northeast orientations of the eddy axes as observed in the standard run have disappeared, suggesting that these asymmetries were due to Rossby waves.

In Fig. 7b we identified three different regimes in the phase speed spectrum. Each of these regimes is typ-

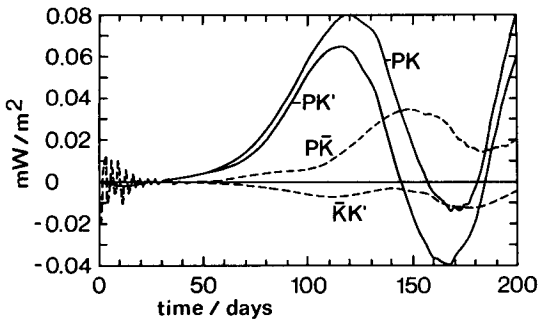

FIG. 8. Energy conversion rates integrated over the total domain. PK: Conversion of potential to kinetic energy, PK̄: Conversion of potential to mean kinetic energy, PK': Conversion of potential to eddy kinetic energy, K̄K': Conversion of mean kinetic to eddy kinetic energy. Negative values indicate conversion in the other direction.

ical for a special class of waves. Regime I is due to topographic Rossby waves traveling to the east (positive phase speeds) along the Cape Verde Plateau. According to LeBlond and Mysak (1978, p. 178ff) such waves can exist in the Northern Hemisphere if the bottom slopes to the north and the e-folding scale of the bottom slope is smaller than $-f_0/\beta'$. These are both true for the Cape Verde Plateau: The e-folding scale is about 1600 km, $f_0 = 4.97 \times 10^{-5}\ s^{-1}$ and $\beta' = -0.152 \times 10^{-10}\ s^{-1}\ m^{-1}$ giving $-f_0/\beta' = 3270$ km. In the flat bottom model, Regime I is not present, which proves that these waves are caused by the topography. Regime II is characterized by fast moving waves traveling west, which we suppose to be barotropic Rossby waves. A 1000 km barotropic Rossby wave should have a theoretical phase speed of -38.5 cm s^{-1}—in the model we find about -30 cm s^{-1} in the bottom layer. The difference is probably caused by a superposition of a topographic Rossby wave having the same wavelength and traveling in the opposite direction. In the model run with a constant Coriolis parameter, Regime II has disappeared and we find, in fact, only positive phase speeds in the bottom layer; the high frequency fluctuations at the low wavenumber end of the spectrum have also disappeared. In the upper layers using constant f, the fast moving waves are also no longer present, proving them to be barotropic Rossby waves. In the flat-bottom model, the waves in Regime I are moving faster westward and this regime is no longer limited to layers below layer 3 (cf. section 3), but can also be found in the surface layers at the low wavenumber end of the spectrum. This can be explained by two effects: first, there is less growth of the baroclinically unstable waves without a sloping bottom, which leads to shorter time scales in this part of the spectrum, and second, the topographic Rossby waves (positive phase speeds) have disappeared. Finally, the rest of the spectrum (Regime III) is occupied by baroclinically unstable waves. Their phase speeds are determined by those found at the "steering level" $H = f_0/(Nk^*)$ (see Gill 1982), where N is the Brunt–Väisälä frequency. For our most unstable wave (200 km long and $N = 10^{-2}\ s^{-1}$), the steering level is located at about 160 m depth or, in σ_θ-units, at roughly the 26.6 kg m^{-3} level. The mean speed there is toward the west and is of order 1 cm s^{-1}, which can be estimated from Fig. 5a. This agrees with our phase speeds found in Regime III. According to Eady's model, the phase speed is given by the real part of (3), i.e., the speed should be half the surface value of the jet velocity, about 5 cm s^{-1} in our model. This value does not match our model value, which is due to (3) valid only for constant vertical shear.

5. Comparisons with observations

There have been just a few observational studies of the CVFZ, and of these only a minority have given results that are comparable with those from our model. Information concerning the spatial scales of variability can be drawn from Hagen and Schemainda (1986) and ZKS. Hagen and Schemainda (1986) calculated the geostrophic meridional velocity along a zonal CTD section extending over nearly 1000 km at 20°10'N between the African shelf and 26°W. Sign changes in the meridional velocity due to eddy motion occurred on horizontal scales of about 100 km, which is comparable to our model predictions (Fig. 5). Similar scales have also been found by ZKS (their Fig. 13). Peak velocities of the jet of up to 20 cm s^{-1} can be found at the sea surface both in our model (Fig. 6) and the observation (ZKS, Fig. 13) and below 400-m depth there are maximum velocities of about 5 cm s^{-1}. Except from the publications of Dantzler (1977) and Cox (1985) we do not have any idea about the width of the eddy containing region between NACW and SACW. Both papers suggest a width of about 500 km, which is close to our model predictions. In situ observations of temporal scales of variability can be obtained only from ZKS: They present temperature and velocity time series from current meters at 400-m depth at different locations in the CVFZ (ZKS, Fig. 17). An inspection of their records led them to conclude that the dominant time scales are shorter than those predicted by this model. For depths near 400 m, the model gives periods between 100 and 150 days, whereas ZKS suggest time scales of 45–75 days.

A comparison of model results with more recent data from mooring site W3 (20°29.6'N, 23°36.6'W, cf. ZKS, Fig. 17) shows better agreement. One-year-records from this mooring have already been included in the ZKS database. Measurements of the horizontal velocities at three different levels at this site are shown in Fig. 9. In the upper (605–700 m) and intermediate (1250–1410 m) levels the time scales of variability are around 100 days, whereas in the deepest level (4500–4505 m) there are shorter time scales also contributing to the spectrum of variability. This is in qualitative agreement with our model results. In order to make quantitative comparisons, we performed a spectral

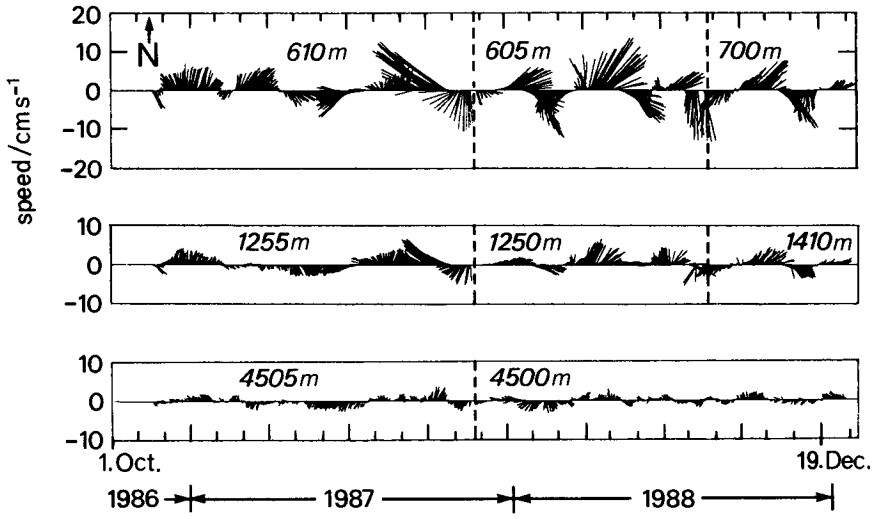

FIG. 9. Observed currents at mooring site W3 (20°29.6'N, 23°36.6'W) at three different levels. Depth changes are due to reinstallation of the mooring or to loss of buoyancy.

analysis from which the results are displayed in Fig. 10. Figure 10a shows the energy density spectrum of the flow field in all three levels. Taking into account the confidence limits we can say that the majority of energy is contained in periods longer than 70 days. An absolute energy maximum can be seen around 100 days in the upper and intermediate level and closer to 200 days in the deepest level. The spectrum in the upper levels can be divided into three regimes: In the long period range greater than 70 days, the energy is distributed equally among all frequencies (plateau regime), between 70 and about 20 days the spectral energy decreases very rapidly, and in the third regime containing periods less than 20 days the spectral slope is smaller. In the deepest layer, however, we can identify only two regimes—a plateau regime and a regime with rather constant spectral slope for the rest of the spectrum, that has nearly the same slope as do the high frequency regimes in the two levels above.

How can we now relate the observed spectra to our model findings? First of all, the periods containing the major part of the energy are consistent with the model predictions. In the model we found the dominant time scales for the depth range of about 600 to 1300 m to be peaked at around 125 days (cf. Fig. 7a,c). Periods shorter than 100 days were found to be very much less energetic, which is not true for longer periods. The same can be found in the observed spectrum, where we find a plateau for periods longer than about 100 days and a very rapid decrease in energy for periods less than 100 days. In the model close to the bottom we found planetary waves to be relatively more important to the high-frequency variability of the flow because of the vanishing influence of the baroclinically unstable waves. Thus, in contrast to the intermediate levels where the major part of spectral energy is contained in the period range greater than about 100 days, there is a weaker decrease of energy levels towards shorter periods, a feature that also exists in the observed spectrum. Here, it should be mentioned that there is a fundamental difference in the procedures used to compute the spectra from the model and the observed data. In the model, we applied the same technique as used by Orlanski and Cox (1973) by decomposing the u'-field in its Fourier components in space and following the characteristic of each independent wave, whereas the observed spectra have been computed by Fourier analysis of a velocity time series at a single point.

In order to clarify whether the observed variability in the CVFZ is caused by baroclinic instability we have computed a spectrum of the phase differences between the upper (605–700 m) and intermediate (1250–1410 m) levels, which is displayed in Fig. 10b. The phases between these two levels are coherent in the period range roughly between 250 and 30 days. This range includes the spectral band which we suppose to be dominated by variability caused by baroclinic instability. Although the error bars suggest the phases are not significantly different from zero, they are all negative in this spectral range, providing evidence that the phases in the intermediate level are leading those in the upper level, which in turn strongly supports the conjecture from our model results that the eddy activity in the CVFZ is due to baroclinic instability.

There remains the question of why the model predictions differ from the observations of ZKS, primarily with respect to time scales. We suppose that one possible source for these differences is that ZKS only estimated the dominant periods from the mooring records. On the other hand, these differences may be caused by the initial conditions used in the model. We have specified our initial fields on the basis of one single CTD-section, which certainly deviates from the mean

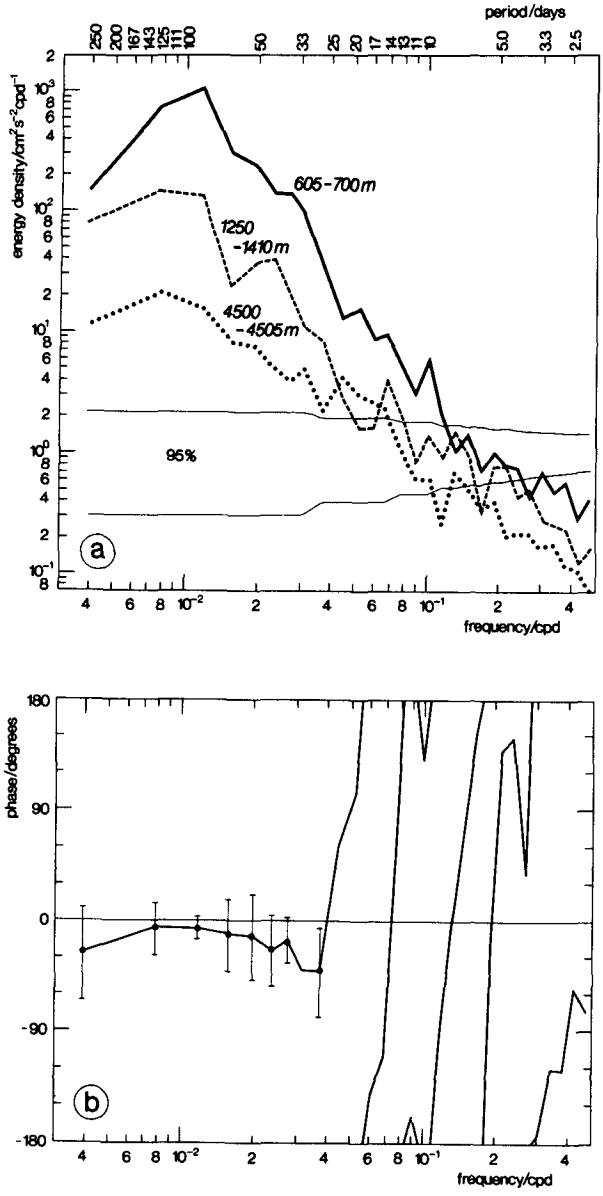

FIG. 10. Spectra of the horizontal currents at mooring site W3. (a) Energy spectrum. Thin lines denote the 95% confidence limits. (b) Phase spectrum between the upper (605–700 m) and the intermediate (1250–1410 m) levels. Positive phase indicates that the upper level is leading. Error bars denote the 95% confidence limits and are drawn only in coherent parts of the spectrum.

climatological situation in this area that has strong seasonal variability (Richardson and Walsh 1986; Picaut 1985; Stramma and Siedler 1988). In formulating the initial conditions, we "unmixed" the measured potential vorticity field and made a guess as to what the initial potential vorticity structure should look like before turbulent mixing takes place. This may be the most crucial point as there are no suitable climatological fields with which to quantitatively compare our potential vorticity field; only qualitative comparisons are possible. This, together with the hyperbolic-tangent approximation of the density field and the jetlike structure of the Canary Current, may lead to an unrealistic flow field at the steering level which determines the propagation speed of meanders and eddies.

6. Conclusions

We have used a three-dimensional numerical model to investigate space and time scales of variability in the Cape Verde Frontal Zone (CVFZ). In the model, meander growth and eddy generation is caused by baroclinic instability. The most unstable wave has a length of 200 km, the spatial scales of detached eddies are 100 km. The instabilities are confined to a 300 km wide zonal strip. They are driven by a sign change of the potential vorticity gradient, which occurs at about 400 m depth. The bottom slope of the Cape Verde Plateau only accelerates the growth of unstable waves and does not provide the main forcing.

We have found the temporal variability to be controlled by three different types of waves: the upper layers (0–200 m) are dominated by baroclinically unstable waves and eddies propagating slowly westward with the Canary Current. These have time scales of about 150 days. Variations in the deep layers (1000 m–bottom) have time scales of less than 50 days to infinity. The short-period variability is due to fast moving Rossby waves traveling to the west, whereas that occurring over long periods is caused by topographic Rossby waves traveling slowly eastward. Finally, in the intermediate layers the most important time scales are between 100 days and infinity with the major part of the energy being contained in the 100 to 125 day period range.

A comparison of our model results with observations reported in different sources shows good agreement with respect to spatial scales, which are also confirmed by Eady's model. Using records that span more than two years from current meters moored in the CVFZ, we have calculated the temporal scales of variability and find them to be consistent with the model results within statistical limits. In our mooring data we also find evidence that baroclinic instability is the physical mechanism leading to the observed variability in the CVFZ.

Acknowledgments. We would like to express our gratitude to T. J. Müller and C. Tietze for processing and analyzing the W3-mooring data and G. Siedler and R. G. Peterson for useful comments on an early version of this paper. We also thank two anonymous referees for excellent reviews. This work was supported by the Deutsche Forschungsgemeinschaft (SFB 133).

REFERENCES

Barton, E. D., 1987: Meanders, eddies, and intrusions in the thermocline front off Northwest Africa. *Oceanol. Acta,* **10,** 267–282.

Bleck, R., 1978: Finite difference equations in generalized vertical coordinates. Part I: Total energy conservation. *Contrib. Atmos. Phys.*, **51**, 360–372.

——, and D. B. Boudra, 1981: Initial testing of a numerical ocean circulation model using a hybrid (quasi-isopycnic) vertical coordinate. *J. Phys. Oceanogr.*, **11**(6), 755–770.

Boudra, D. B., R. Bleck and F. Schott, 1988: A numerical model of instabilities of the Florida Current. *J. Mar. Res.*, **46**, 715–751.

Cox, M. D., 1985: An eddy resolving model of the ventilated thermocline. *J. Phys. Oceanogr.*, **15**, 1312–1324.

Dantzler, H. L., 1977: Potential energy maxima in the tropical and subtropical Atlantic. *J. Phys. Oceanogr.*, **7**, 512–519.

Emery, W. J., and J. Meincke, 1986: Global water masses: summary and review. *Oceanol. Acta*, **9**(4), 383–391.

——, W. G. Lee and L. Magaard, 1984: Geographic and seasonal distributions of Brunt-Väisälä frequency and Rossby radii in the North Pacific and North Atlantic. *J. Phys. Oceanogr.*, **14**(2), 294–317.

Gill, A. E., 1982: *Atmosphere–Ocean Dynamics.* Academic Press, 662 pp.

Hagen, E., and R. Schemainda, 1986: On actual and climatological vertical structures within the 1500 dbar top layer northwest off Cape Verde Islands. *Beitr. Meeresk.*, **55**, 19–27.

Haidvogel, D. B., 1983: Periodic and regional models. *Eddies in Marine Science,* A. Robinson, Ed., Springer Verlag, 404–437.

Hide, R., and P. J. Mason, 1975: Sloping convection in a rotating fluid. *Advances in Physics,* vol. 24, Academic Press, 47–100.

Hoskins, B. J., M. E. McIntyre and A. W. Robertson, 1985: On the use and significance of isentropic potential vorticity maps. *Quart. J. Roy. Meteor. Soc.*, **111**, 877–946.

Ikeda, M., 1983: Linear instability of a current flowing along a bottom slope using a three layer model. *J. Phys. Oceanogr.*, **13**(2), 208–223.

Keffer, T., 1985: The ventilation of the world's oceans: maps of the potential vorticity field. *J. Phys. Oceanogr.*, **15**, 509–523.

LeBlond, P. H., and L. A. Mysak, 1978: *Waves in the Ocean.* Elsevier Scientific, 602 pp.

Luyten, J. R., J. Pedlosky and H. Stommel, 1983: The ventilated thermocline. *J. Phys. Oceanogr.*, **13**, 292–309.

Manríquez, M., and F. Fraga, 1982: The distribution of water masses in the upwelling region off Northwest Africa in November. *Rapp. P.-v. Réun. Cons. Int. Explor. Mer*, **180**, 39–47.

McDowell, S., P. B. Rhines and T. Keffer, 1982: North Atlantic potential vorticity and its relation to the general circulation. *J. Phys. Oceanogr.*, **12**(12), 1417–1436.

Mechoso, C. R., and D. M. Sinton, 1981: Instability of baroclinic flows with horizontal shear along topography. *J. Phys. Oceanogr.*, **11**(6), 813–821.

Orlanski, I., 1969: The influence of bottom topography on the stability of jets in a baroclinic fluid. *J. Atmos. Sci.*, **266**(6), 1216–1232.

——, and M. D. Cox, 1973: Baroclinic instability in ocean currents. *Geophys. Fluid Dyn.*, **4**, 297–392.

Pedlosky, J., 1979: *Geophysical Fluid Dynamics.* Springer Verlag, 624 pp.

Picaut, J., 1985: Major dynamics affecting the eastern tropical Atlantic and Pacific oceans. Calif. Coop. Ocean. Fish. Invest. (Ser. Reps.), **26**, 41–50.

Richardson, P. L., 1983: Eddy kinetic energy in the North Atlantic from surface drifters. *J. Geophys. Res.*, **88**, 4355–4367.

——, and D. Walsh, 1986: Mapping climatological seasonal variations of surface currents in the tropical Atlantic using ship drifts. *J. Geophys. Res.*, **91**(C9), 10 537–10 550.

Stramma, L., and G. Siedler, 1988: Seasonal changes in the North Atlantic Subtropical Gyre. *J. Geophys. Res.*, **93**(C7), 8111–8118.

Sverdrup, H. U., M. W. Johnson and R. H. Fleming, 1942: *The Oceans.* Prentice Hall, 1087 pp.

Zenk, W., B. Klein and M. Schröder, 1990: Cape Verde Frontal Zone. *Deep-Sea Res.*, in press.